Interstitial Doping of SnO_2 Film with Li for Indium-Free Transparent Conductor

Xingqian Chen(陈兴谦)[1,2,5], Haozhen Li(李昊臻)[1,2,5], Wei Chen(陈伟)[2,4], Zengxia Mei(梅增霞)[1,2], Alexander Azarov[3], Andrej Kuznetsov[3], and Xiaolong Du(杜小龙)[1,2,4*]

[1]*Beijing National Laboratory for Condensed Matter Physics, and Institute of Physics, Chinese Academy of Sciences, Beijing 100190, China*
[2]*Songshan Lake Materials Laboratory, Dongguan 523808, China*
[3]*Department of Physics, Centre for Materials Science and Nanotechnology, University of Oslo, P.O. Box 1048, Blindern, N-0316 Oslo, Norway*
[4]*Guangdong SinoPrime Technology Co., Ltd., Dongguan 523808, China*
[5]*School of Physical Sciences, University of Chinese Academy of Sciences, Beijing 100049, China*

(Received 22 January 2024; accepted manuscript online 11 March 2024)

SnO_2 films exhibit significant potential as cost-effective and high electron mobility substitutes for In_2O_3 films. In this study, Li is incorporated into the interstitial site of the SnO_2 lattice resulting in an exceptionally low resistivity of $2.028 \times 10^{-3}\,\Omega$·cm along with a high carrier concentration of $1.398 \times 10^{20}\,cm^{-3}$ and carrier mobility of $22.02\,cm^2/V{\cdot}s$. Intriguingly, Li_i readily forms in amorphous structures but faces challenges in crystalline formations. Furthermore, it has been experimentally confirmed that Li_i acts as a shallow donor in SnO_2 with an ionization energy ΔE_{D1} of $-0.4\,eV$, indicating spontaneous occurrence of Li_i ionization.

DOI: 10.1088/0256-307X/41/3/037305

Currently, transparent conductive oxide (TCO) films prepared below 200 ℃ received increased attention due to the widespread application of temperature sensitive component in some devices, such as amorphous hydrogenated silicon in Si-heterojunction solar cells or polyvinyl alcohol in flexible optoelectronic devices.[1–6] Indium oxide (In_2O_3), tin dioxide (SnO_2), and zinc oxide (ZnO) films are promising and technologically important TCO films in these applications. Wherein, indium tin oxide (ITO) films have been preferred in industry because of its excellent optical and electrical properties. However, the fact that indium is rare on earth limits its further applications. In addition, although doped ZnO films also presents excellent performance, they are also excluded from the options due to their poor chemical stability,[7] which greatly increases the difficulty of device encapsulation. Therefore, increasing attention is paid to SnO_2, especially the F-doped SnO_2 (FTO) films with outstanding optical and electrical performance, low cost, and chemical and environmental stability.

Among various preparation techniques, magnetron sputtering is expected to be the most suitable for depositing high-quality, well-adhered, and large-sized films at relatively low substrate temperature.[8] For instance, Morán-Pedroso *et al.* reported FTO films deposited at room temperature by sputtering in an atmosphere containing H_2 with optimized sheet resistance of $\sim 20\,\Omega/\square$.[9] Zhu *et al.*[10] obtained minimum resistivity of $8.5 \times 10^{-3}\,\Omega$·cm for FTO films prepared at 150 ℃ and 300 ℃. Wu *et al.*[11] obtained an FTO film with low resistivity of $5.4 \times 10^{-3}\,\Omega$·cm.

In order to further enhance the optical and electrical performance of SnO_2 films, it is imperative to explore donor impurities in SnO_2 that are shallower than F_O. This study reveals that Li, with a smaller radius, when incorporated into the interstitial site of amorphous SnO_2 film, exhibits excellent donor characteristics despite being traditionally considered as an acceptor in crystalline SnO_2.[12] The LiTO films were prepared at 180 ℃ by magnetron sputtering using a $Li_{0.01}Sn_{0.99}O_2$ target in an $Ar + O_2$ atmosphere to investigate the behavior of Li doping in SnO_2 as well as the optical and electrical properties of the resulting LiTO film. Remarkably, we achieved simultaneous enhancements in carrier concentration n ($1.398 \times 10^{20}\,cm^{-3}$), mobility μ ($22.02\,cm^2/V{\cdot}s$), and resistivity ρ ($2.028 \times 10^{-3}\,\Omega$·cm) on the LiTO film. Interestingly, we observed that Li_i formation and consequently electrical performance are significantly influenced by the crystallinity of LiTO films. Specifically, Li_i is more likely to form in amorphous structures but less likely to form in crystalline ones. Consequently, amorphous films consistently exhibit superior electrical performance compared to their crystalline counterparts. Furthermore, we have confirmed that Li_i acts as a shallow donor impurity within SnO_2 with an ionization energy ΔE_{D1} of $-0.4\,eV$, indicating spontaneous occurrence of Li_i ionization.

LiTO films were fabricated on quartz glass substrates at 180 ℃ by magnetron sputtering using $Li_{0.01}Sn_{0.99}O_2$ targets. LiTO films with different thicknesses were prepared at different deposition times of 28, 42, and 70 min, named as LiTO1, LiTO2, and LiTO3, respectively. In addition, a SnO_2 film was prepared for comparison using a SnO_2 target. The diameters of the targets were two inches. The bare pressure of the sputtering chamber was 1.2×10^{-4} Pa and the sputtering was performed at 0.4 Pa under a mixed atmosphere of Ar (99.1%) and O_2 (0.9%).

*Corresponding author. Email: xldu@iphy.ac.cn
© 2024 Chinese Physical Society and IOP Publishing Ltd

All the targets were powered at 30 W and placed 10 cm away from the substrates. The quartz glass substrates were ultrasonically cleaned in acetone, alcohol, and deionized water for 15 min in sequence, and the targets were pre-sputtered for 5 min to remove any contaminant from the target surface before films deposited on the substrates. The substrate temperature was set to 180 ℃ during film growth.

Composition of films were measured by x-ray photoelectron spectroscopy (XPS). The crystal structure of films was characterized by x-ray diffraction (XRD). Thickness and surface morphology of thin films were determined by an atomic force microscope. An infrared (UV-vis-NIR) spectrophotometer was used to measure the optical properties, and Hall measurements (Ecopia HMS-3000) were performed to test resistivity, carrier concentration, and mobility of films. Ultraviolet photoelectron spectra (UPS) were performed to characterize Fermi level and valance band of selected thin films.

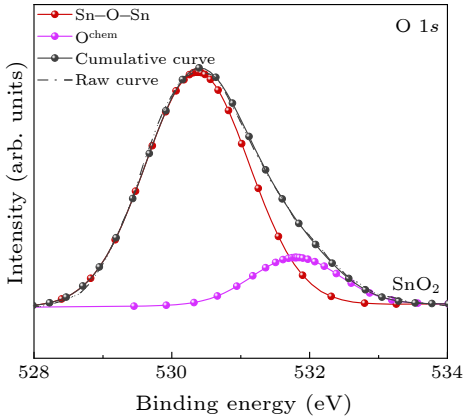

Fig. 1. XPS spectra in the O 1*s* region for SnO_2 films.

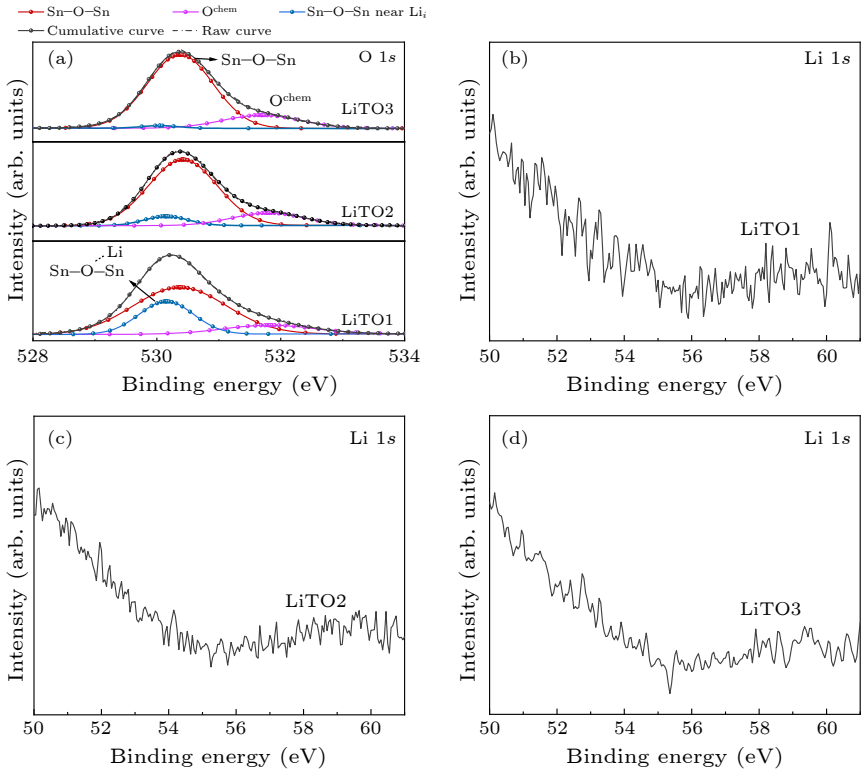

Fig. 2. (a) XPS spectra in the O 1*s* region for LiTO films and Li 1*s* region for (b) LiTO1, (c) LiTO2, and (d) LiTO3 films.

To understand the chemical bonding state of the films, the typical core level XPS spectra are shown in Figs. 1 and 2. All the bonding energies are corrected based on 284.8 eV of C 1*s*. Figure 1 shows a broad asymmetric curve of O 1*s* spectrum, which was fitted by two peaks for the SnO_2 film with binding energies centered at 530.37 eV and 531.8 eV typically ascribed to O–Sn^{4+} and O chemically adsorbed on the surface, respectively.[13,14] A new peak centered at 530.15 eV must be deconvoluted to fit convergence for LiTO films as shown in Fig. 2(a), which can be attributed to Sn–O–Sn in the vicinity of interstitial Li (Li_i). The binding energy decrease can be attributed to both attraction between Li and O and repulsion between Li and Sn. Furthermore, the peak intensity decreases significantly, indicating Li_i content decreasing. Moreover, in the Li 1*s* spectrum shown in Figs. 2(b), 2(c), and 2(d), interestingly, there is no signal at all in this region for LiTO films, meaning that Li_i in SnO_2 is hard to be detected with the XPS spectrum. Therefore, assuming that Li only has a profound impact on the bond energy of the nearest Sn–O–Sn bond, the content of Li can be estimated based on the area of the 530.15 eV peak and the results are summarized in Table 1.

Table 1 shows the element composition for SnO_2 and

LiTO films. From the table, the content of Li in LiTO1 film is 3.14 at.%, which significantly decreases to 0.89 at.% of LiTO2 and 0.21 at.% of LiTO3. In addition, although O_2 was added during film growing, the O/Sn atomic ratio of SnO_2 is 1.90 ascribed to ion bombardment. The ratio is 2.04 for LiTO1, which indicates fewer oxygen vacancies (V_O). Surprisingly, the ratio decreases to 1.87 of LiTO2 and 1.83 of LiTO3 as Li_i content decreases, which can be attributed to their lager deposition rate (2.17 nm/min of LiTO2 and 2.19 nm/min of LiTO3) compared to 1.75 nm/min of SnO_2 and 1.79 nm/min of LiTO1, leading to less time to be oxidized by additional O_2 in the deposition chamber. Furthermore, the large O/Sn ratio difference between SnO_2 and LiTO1 films under similar deposition rates can be attributed to the presence of Li_i in SnO_2, which inhibits the formation of V_O.

Table 1. The element content measured by XPS, thickness, and roughness for SnO_2 and LiTO films. Rq: the root mean square value of sample surface height within the testing area.

Film	Chemical composition (at.%)				Thickness (nm)	Rq (nm)
	Sn	O	Li	O/Sn		
SnO_2	34.54	65.46	–	1.90	77	0.673
LiTO1	31.83	65.03	3.14	2.04	50	0.509
LiTO2	34.54	64.57	0.89	1.87	90	0.526
LiTO3	35.32	64.47	0.21	1.83	150	0.575

Table 2. The electrical and optical performance of SnO_2 and LiTO films measured at 25 ℃.

Film	n (10^{20}/cm^3)	μ (cm^2/V·s)	ρ (10^{-3} Ω·cm)	$\bar{\alpha}$ ($\times 10^{-4}$ nm^{-1})	E_g (eV)
SnO_2	–	–	–	2.39	3.45
LiTO1	1.398	22.02	2.028	5.46	3.63
LiTO2	0.646	17.42	5.548	2.36	3.74
LiTO3	0.307	11.43	17.780	1.97	3.81

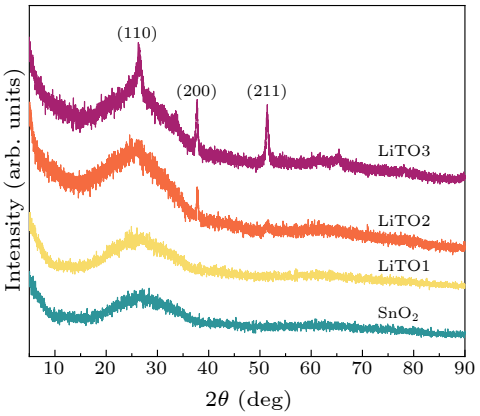

Fig. 3. The XRD patterns of SnO_2 and LiTO films.

Figure 3 presents the x-ray diffraction patterns of all films over the 2θ, ranging from 5° to 90°. It can be seen that SnO_2 film presents an amorphous structure. In addition, LiTO1 is also amorphous due to its thin thickness. Expectedly, (200) and (211) peaks located at 37.9° and 51.8° (PDF card: No. 41–1445), respectively, appear for LiTO2, and intensity of the two peaks further increases along with the appearance of another (110) peak centered at 33.9° (PDF card: No. 41–1445) for LiTO3, which means that the crystallinity of the films increases as the film thickness increases. Moreover, Li compounds are doped into host SnO_2 lattice or amorphous since no other diffraction peaks can be detected. Surprisingly, there is a strong correlation between the Li_i content and the crystallinity. Specifically, the lower the crystallinity, the higher the Li_i content in the film. In the amorphous state, only the first-shell corresponds to the nearest Sn–O bonds. In a longer range, all structural features are suppressed, and thus the amorphous structure of SnO_2 can be regarded as a random combination of nearest neighbor Sn–O structures. These combinations, like In_2O_3, are also composed of face-shared, edge-shared, corner-shared, and non-shared types.[15] The combinations of corner-shared and non-shared types will produce some large-sized interstitial sites, leading to easier formation of Li_i. However, for SnO_2 with a crystalline rutile structure, even the size of the largest octahedral interstitial site of 72 pm is smaller than the diameter of Li^+ (120 pm), making it difficult to form Li_i. Therefore, the low crystallinity of LiTO with high Li content can be attributed to the lower formation energy of Li_i in amorphous crystals. In addition, the interaction between Li_i and its nearest neighboring Sn–O bonding will further reduce the formation energy of Li_i and improve its stability.

Furthermore, to investigate electrical performance evolution, carrier concentration n, mobility μ, and resistivity ρ of SnO_2 and LiTO films are measured and summarized in Table 2. The SnO_2 film is almost insulated and its resistivity exceeds the range of the Hall measurement. Surprisingly, LiTO1 film exhibits an extremely low resistivity of 2.028×10^{-3} Ω·cm and high μ of 22.02 cm^2/V·s. This high mobility can be ascribed to its insensitiveness to the distorted Sn–O–Sn chemical bonds originated from the magnitude of isotropic neighbouring Sn 5s orbitals overlap.[16] Due to few V_O in the film suggested by the high O/Sn ratio as shown in Table 1, it can be rationally concluded that Li_i with very small activation energy mainly causes the conductivity of the film. Moreover, resistivity ρ increases to 5.548×10^{-3} Ω·cm for LiTO2 and further increases to 17.780×10^{-3} Ω·cm for LiTO3 with reduced Li_i content. It is worth noting that the film mobility continues to decrease with the optimization of film crystallinity. As for LiTO2 film, due to the coexistence of (200) ori-

ented crystalline grains and amorphous phases, electrons are subject to interface scattering during transport between amorphous and crystalline grains, resulting in a decrease in electron mobility to 17.42 $cm^2/V{\cdot}s$. Furthermore, when electrons are transported between amorphous phase and crystalline grains, as well as crystal grains with different orientations, they are subjected to significant interface scattering effects, resulting in a further decrease in the electron mobility to 11.43 $cm^2/V{\cdot}s$ of LiTO3 film. In addition, compared with ITO films prepared under the similar conditions with resistivity of about $2 \times 10^{-3}\,\Omega{\cdot}cm$,[17] LiTO films exhibit competitive electrical resistivity and even higher carrier concentration, which suggests that it is entirely possible for LiTO films to replace expensive ITO films in low-temperature applications, especially under conditions below 200 ℃.

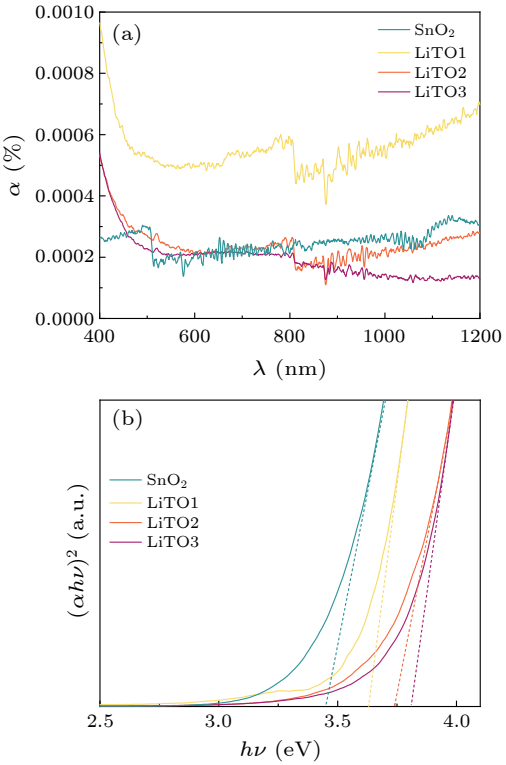

Fig. 4. (a) Optical absorption coefficient and (b) optical band gap of SnO_2 and LiTO films.

In addition, the optical absorption coefficients α of SnO_2 and LiTO films as a function of wavelength are shown in Fig. 4(a) to eliminate the influence of film thickness for better optical performance comparison. Meanwhile, the mean absorption coefficient $\bar{\alpha}$ are calculated by[18]

$$\bar{S} = \frac{\int_{400\,\mathrm{nm}}^{1200\,\mathrm{nm}} S(\lambda)\Gamma(\lambda)d\lambda}{\int_{400\,\mathrm{nm}}^{1200\,\mathrm{nm}} \Gamma(\lambda)d\lambda}, \tag{1}$$

where $\Gamma(\lambda)$ and $S(\lambda)$ represent the standard AM1.5 solar photon spectral distribution and the experimental absorption coefficient as shown in Fig. 4(a). The calculation results are summarized in Table 2. The absorption coefficient of SnO_2 sample is quite low, and the average absorption coefficient is $2.39 \times 10^{-4}\,nm^{-1}$. For LiTO1 film, a high $\bar{\alpha}$ of $5.46 \times 10^{-4}\,nm^{-1}$ as a result of the plasmon absorption caused by high carrier concentration is presented. Furthermore, as the thickness of the film increases, the Li_i content in the film decreases, and thus the carrier concentration decreases, resulting in a decrease of absorption as shown in Fig. 4(a) and decline of $\bar{\alpha}$ to $2.36 \times 10^{-4}\,nm^{-1}$ for LiTO2 and $1.97 \times 10^{-4}\,nm^{-1}$ for LiTO3. Moreover, the change in photon energy $h\nu$ and optical absorption coefficient (α) for the SnO_2 and LiTO films are displayed in Fig. 4(b) to extract optical band gap according to the following relation:[18] $(\alpha h\nu)^2 = A(h\nu - E_g)$, where A is a constant. The extracted optical band gap is summarized in Table 2. The E_g of SnO_2 is 3.45 eV, which is smaller than reported 3.6 eV[19] attributed to numerous V_O. For the LiTO films, the Burstein–Moss effect, lattice distortion caused by interstitial Li doping, film thickness, and crystallinity would have a profound impact on the bandgap of the films.[20,21] The $\Delta E_{g,\,BM}$ resulted from the Burstein–Moss effect can be calculated by the following relationship:[21]

$$\Delta E_{g,BM} = \frac{h^2}{8m^*\pi^2}(3\pi^2 n)^{2/3}, \tag{2}$$

where h is Planck's constant, m^* is the reduced effective mass that is $0.3m_0$ for SnO_2. In addition, the crystallinity of the films can be evaluated using the grain size calculated by the Debye–Scherrer formula[22] utilizing full width at half maximum of XRD diffraction peaks, and the estimated grain sizes of LiTO2 and LiTO3 are 14.9 nm and 22.4 nm, respectively.

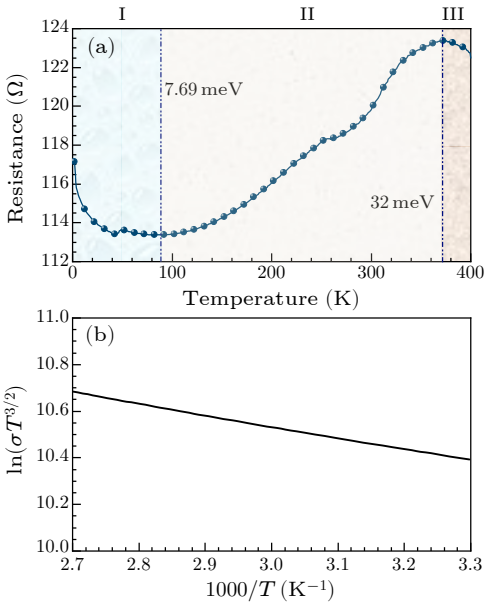

Fig. 5. (a) Resistance variation with temperature and (b) plot of $\ln(\sigma T^{3/2})$ versus $1000/T$ of LiTO1 film.

Considering that the SnO_2 and LiTO1 films are both amorphous, the influence of crystallinity on the band gap can be supposed to be the same. Meanwhile, the calculated $\Delta E_{g,\,BM}$ of LiTO1 is 0.33 eV and a bandgap reduction of ∼0.1 eV due to the small thickness in comparison with SnO_2 film based on Ref. [20]. Therefore, the band gap reduction resulting from lattice distortion caused by interstitial Li doping is estimated to be 0.05 eV, which is not

obvious. It can be reasonably ignored in the case of LiTO2 and LiTO3 films with much low Li content. Furthermore, the calculated $\Delta E_{\mathrm{g,\,BM}}$ values for LiTO2 and LiTO3 are 0.2 eV and 0.12 eV, respectively. When the thickness of the film exceeds 79 nm, the influence of film thickness on the bandgap of the film is significantly reduced and the thicker thickness only increases the bandgaps of LiTO2 and LiTO3 films by approximately 0.01 eV and 0.04 eV, respectively, compared to SnO_2 based on Ref. [20]. Therefore, the significant optimization of the crystallinity of the film at this time plays a major role in bandgap increasement of the both films. Finally, the crystalline effects for LiTO2 and LiTO3 films are estimated to be 0.08 eV and 0.2 eV, respectively.

The resistance of LiTO1 film in the temperature range 1.9–400 K are shown in Fig. 5. The film resistance varies with temperature in three stages: The characteristic of stage I is that the resistance decreases with increasing temperature. This can be ascribed to that as the temperature increases, the Li_i donor impurity is excited, the carrier concentration increases, and the mobility is controlled by ionized impurity scattering, which also increases with increasing temperature. It is not until 89 K that the donor impurity is fully excited, and the mobility is equivalent to lattice vibration scattering by ionized impurity scattering. In stage Ⅱ, the donor impurity is fully excited and the mobility changes from dominated by ionized impurity scattering to dominated by lattice vibration scattering. As the temperature increases, the mobility decreases and the resistance increases until 371 K, and the intrinsic excitation effect becomes apparent. The intrinsic excitation mechanism in stage Ⅲ is dominant, and as the temperature increases, the carrier concentration increases and the resistance decreases.

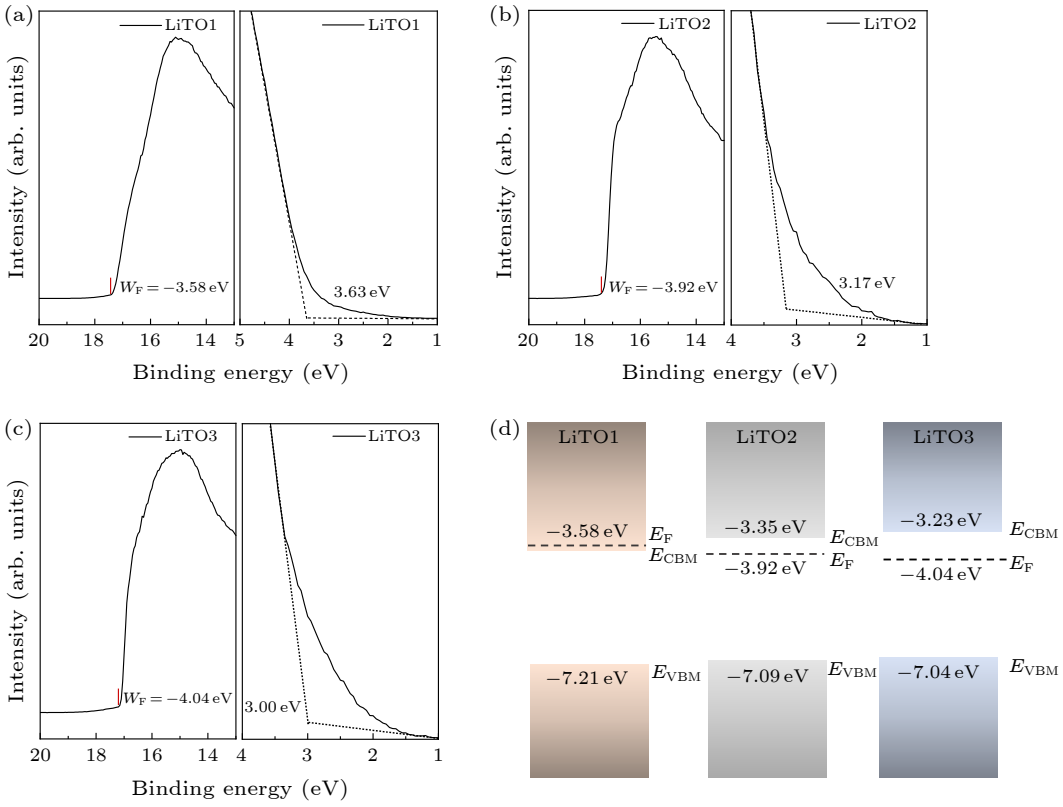

Fig. 6. UPS spectra of (a) LiTO1, (b) LiTO2, and (c) LiTO3 films, and (d) energy band structure diagrams of LiTO1, LiTO2, and LiTO3 films.

Furthermore, the defects in the LiTO1 film are Li_i and $\mathrm{V_O}$. Therefore, the ionization reaction of these defects can be written in the following form:

$$\mathrm{Li}_i \rightleftharpoons \mathrm{Li}_i^+ + e, \tag{3}$$

$$V_{\mathrm{O}} \rightleftharpoons V_{\mathrm{O}}^+ + e, \tag{4}$$

$$V_{\mathrm{O}} \rightleftharpoons V_{\mathrm{O}}^{++} + 2e. \tag{5}$$

According to the mass action equilibrium formulas, they have the following relationship:

$$\frac{[\mathrm{Li}_i^+]n}{[\mathrm{Li}_i]} = A_1 \exp(-\Delta E_{\mathrm{D1}}/kT), \tag{6}$$

$$\frac{[V_{\mathrm{O}}^+]n}{[V_{\mathrm{O}}]} = A_2 \exp(-\Delta E_{\mathrm{D2}}/kT), \tag{7}$$

$$\frac{[V_{\mathrm{O}}^{++}]n^2}{[V_{\mathrm{O}}]} = A_3 \exp(-\Delta E_{\mathrm{D3}}/kT). \tag{8}$$

Here, n is also the carrier concentration. $[\mathrm{Li}_i^+]$, $[V_{\mathrm{O}}^+]$, and $[V_{\mathrm{O}}^{++}]$ are the ionized defect concentrations. $[\mathrm{Li}_i]$ and $[V_{\mathrm{O}}]$ are the concentrations of Li_i and $\mathrm{V_O}$, respectively. ΔE_{D1}, ΔE_{D2}, and ΔE_{D3} are ionization energies of relevant reac-

tions. A1, A2, and A3 are pre-exponentials of the reactions. On this basis, according to Ref. [23], the conductivities of LiTO1 film are given as

$$\sigma = \frac{e\mu_0}{T^{3/2}}\left\{(N_{\mathrm{D1}}^{\mathrm{Li}}A_1)^{1/2}\exp\left[\frac{-E_{\mathrm{H}}^{\mathrm{Li}}-\frac{\Delta E_{\mathrm{D1}}}{2}}{kT}\right] + (N_{\mathrm{D2}}^{\mathrm{Li}}A_2)^{1/2}\exp\left[\frac{-E_{\mathrm{H}}^{\mathrm{Li}}-\frac{\Delta E_{\mathrm{D2}}}{2}}{kT}\right]\right\}, \quad (9)$$

where $N_{\mathrm{D1}}^{\mathrm{Li}}$ and $N_{\mathrm{D2}}^{\mathrm{Li}}$ represent the concentrations of doped Li and singly ionized oxygen vacancy, respectively; k is Boltzmann's constant; μ_0 is another pre-exponential factor. $E_{\mathrm{H}}^{\mathrm{Li}}$ is the electron hopping energy, which is 0.242 eV reported in Ref. [23]. In this work, it can be determined that there is almost no V_{O} in the LiTO1 film from the O/Sn ration of 2.04, and high concentration of electrons from the ionization of Li_i can further suppress reactions (4) and (5), which leads to a negligible $N_{\mathrm{D2}}^{\mathrm{Li}}$. Therefore, there exists the following relationship for LiTO1 film:

$$\ln(\sigma T^{\frac{3}{2}}) = \ln\left[e\mu_0(N_{\mathrm{D1}}^{\mathrm{Li}}A_1)^{\frac{1}{2}}\right] - \frac{E_{\mathrm{H}}^{\mathrm{Li}}+\frac{\Delta E_{\mathrm{D1}}}{2}}{1000k}\frac{1000}{T}. \quad (10)$$

The ionization energy ΔE_{D1} of Li_i can be determined from $\ln(\sigma T^{3/2})$ plot versus $1000/T$, as shown in Fig. 5(b). The slope of the straight line in the figure is -0.49, deducing a ΔE_{D1} of -0.4 eV, which is less than 0, meaning that Li_i ionization always occurs spontaneously.

To further illustrate the physical mechanisms of optical and electrical performance evolution, energy levels of LiTO films are investigated using UPS. Figure 6 shows the secondary electron cutoff region representative for the W_{F} and the valance band (VB) edges of LiTO films. The exact VB offset is determined by extrapolating the leading edge of the VB spectrum to the base line. The W_{F} of LiTO1 ($W_{\mathrm{F}} = -3.58$ eV) slightly shifted toward a higher energy by 0.34 eV as compared to LiTO2 ($W_{\mathrm{F}} = -3.92$ eV), and 0.46 eV as compared to LiTO3 ($W_{\mathrm{F}} = -4.04$ eV), which conforms well the carrier concentration n. Also, based on the UPS spectra and the optical bandgap E_{g} shown in Table 2, the relevant energy band structure diagrams are constructed in Fig. 6(d).

In summary, we have investigated the structure and properties of low-temperature sputtered LiTO films. Two significant conclusions can be proposed: (i) Li_i tends to form easily in amorphous structures but faces difficulties in crystalline formations. (ii) Li_i acts as a shallow donor in SnO_2, with an estimated ionization energy ΔE_{D1} of -0.4 eV, indicating spontaneous occurrence of Li_i ionization. Consequently, the LiTO film simultaneously achieves excellent resistivity of $2.028 \times 10^{-3}\,\Omega\cdot$cm, accompanied by high carrier concentration of $1.398 \times 10^{20}\,\mathrm{cm}^{-3}$ and carrier mobility of $22.02\,\mathrm{cm}^2/\mathrm{V}\cdot\mathrm{s}$. The present study is expected to contribute significantly to the advancement of low-temperature magnetron sputtering for the growth of doped SnO_2 transparent conductive films, thereby yielding substantial benefits in their applications.

Acknowledgments. This work was supported by the Key-Area Research and Development Program of Guangdong Province (Grant No. 2021B0101260001), the Guangdong Basic and Applied Basic Research Foundation (Grant No. 2019A1515110411), and partly the INTPART Program at the Research Council of Norway (Grant No. 322382).

References

[1] Yu C, Zou Q, Wang Q, Zhao Y, Ran X, Dong G, Peng C W, Allen V, Cao X, Zhou J, Zhao Y, and Zhang X 2023 *Nat. Energy* **8** 1119
[2] Zheng J, Ying Z, Yang Z, Lin Z, Wei H, Chen L, Yang X, Zheng Y, Li X, and Ye J 2023 *Nat. Energy* **8** 1250
[3] Yu C, Gao K, Peng C W, He C R, Wang S B, Shi W, Allen V, Zhang J, Wang D Z, Tian G Y, Zhang Y, Jia W, Song Y, Hu Y, Colwell J, Xing C, Ma Q, Wu H, Guo L, Dong G, Jiang H, Wu H, Wang X, Xu D, Li K, Peng J, Liu W, Chen D, Lennon A, Cao X, De Wolf S, Zhou J, Yang X, and Zhang X 2023 *Nat. Energy* **8** 1375
[4] Lin H, Yang M, Ru X N, Wang G S, Yin S, Peng F G, Hong C J, Qu M H, Lu J, Fang L, Han C, Procel P, Isabella O, Gao P, Li Z, and Xu X 2023 *Nat. Energy* **8** 789
[5] Chen Z, Wang J, Wu H B, Yang J M, Wang Y K, Zhang J, Bao Q Y, Wang M, Ma Z F, Tress W, and Tang Z 2022 *Nat. Commun.* **13** 4387
[6] Shi J L, Zhang J Y, Yang L, Qu M, Qi D C, and Zhang K H L 2021 *Adv. Mater.* **33** 2006230
[7] Tung H T, Nguyen T P, Huu P D, and Le T 2021 *Surf. Interfaces* **23** 100943
[8] Zhu B L, Liu F, Li K, Lv K, Wu J, Gan Z H, Liu J, Zeng D W, and Xie C S 2017 *Ceram. Int.* **43** 10288
[9] Morán-Pedroso M, Gago R, Julin J, Salas-Colera E, Jimenez I, de Andrés A, and Prieto C 2021 *Appl. Surf. Sci.* **537** 147906
[10] Zhu B L, Zhao X, Hu W C, Li T T, Wu J, Gan Z H, Liu J, Zeng D W, and Xie C S 2017 *J. Alloys Compd.* **719** 429
[11] Wu F Y, Tong X R, Zhao Z, Gao J B, Zhou Y W, and Kelly P 2017 *J. Alloys Compd.* **695** 765
[12] Wang J C, Zhou W, and Wu P 2014 *Appl. Surf. Sci.* **314** 188
[13] Yousaf M U, Pervaiz E, Minallah S, Afzal M J, Honghong L, and Yang M 2019 *Results Phys.* **14** 102455
[14] Hernández-Gutiérrez C A, Vigil G O, Melo S, Rodriguez E, and Kudriavtsev Y 2019 *Rev. Mex. Fís.* **65** 554
[15] Medvedeva J E, Buchholz D B, and Chang R P H 2017 *Adv. Electron. Mater.* **3** 1700082
[16] Nomura K, Ohta H, Takagi A, Kamiya T, Hirano M, and Hosono H 2004 *Nature* **432** 488
[17] Guillén C and Herrero J 2007 *J. Appl. Phys.* **101** 073514
[18] Ramarajan R, Kovendhan M, Thangaraju K, Joseph D P, Babu R R, and Elumalai V 2020 *J. Alloys Compd.* **823** 153709
[19] Akgul F A, Gumus C, Er A O, Farha A H, Akgul G, Ufuktepe Y, and Liu Z 2013 *J. Alloys Compd.* **579** 50
[20] Zhang M, Xu M, Li M, Zhang Q, Lu Y, Chen J, Li M, Dai J, Chen C, and He Y 2017 *Appl. Surf. Sci.* **423** 611
[21] So H S, Park J W, Jung D H, Ko K H, and Lee H 2015 *J. Appl. Phys.* **118** 085303
[22] Patterson A L 1939 *Phys. Rev.* **56** 978
[23] Zhang G Z, Xie C S, Zhang S P, Zhang S S, and Xiong Y 2014 *J. Phys. Chem. C* **118** 18097